

First-principles calculations of ^{17}O NMR chemical shielding in $\text{Pb}(\text{Zr}_{1/2}\text{Ti}_{1/2})\text{O}_3$ and $\text{Pb}(\text{Mg}_{1/3}\text{Nb}_{2/3})\text{O}_3$: linear dependence on transition-metal/oxygen bond lengths

Daniel L. Pechkis, Eric J. Walter and Henry Krakauer

Department of Physics, College of William and Mary, Williamsburg, VA 23187-8795.

(Dated: July 26, 2011)

First-principles density functional theory (DFT) oxygen chemical shift tensors were calculated for $\text{A}(\text{B},\text{B}')\text{O}_3$ perovskite alloys $\text{Pb}(\text{Zr}_{1/2}\text{Ti}_{1/2})\text{O}_3$ (PZT) and $\text{Pb}(\text{Mg}_{1/3}\text{Nb}_{2/3})\text{O}_3$ (PMN). Quantum chemistry methods for embedded clusters and the GIPAW method [C. J. Pickard and F. Mauri, *Phys. Rev. B* **63** 245101 (2001)] for periodic boundary conditions were used. Results from both methods are in good agreement for PZT and prototypical perovskites. PMN results were obtained using only GIPAW. Both isotropic δ_{iso} and axial δ_{ax} chemical shifts were found to vary approximately linearly as a function of the nearest-distance transition-metal/oxygen bond length, r_s . Using these results, we argue against Ti clustering in PZT, as conjectured from recent ^{17}O NMR magic-angle-spinning measurements. Our findings indicate that ^{17}O NMR measurements, coupled with first-principles calculations, can be an important probe of local structure in complex perovskite solid solutions.

PACS numbers: 76.60.Cq 77.84.-s

I. INTRODUCTION

High performance solid solution ferroelectrics, based on the ideal ABO_3 perovskite structure, are widely used in technological applications such as ultrasonic transducers, sensors, actuators, and thin film applications.^{1,2} The strong electromechanical coupling in these materials is related to a balance of competing instabilities, such as cation off-centerings and oxygen octahedral rotations. The perovskite structure offers many ways to fine tune these interactions through chemical substitutions, such as alloying on the A and/or B sites, and through epitaxial control in layered and thin film geometries.¹

Solid state nuclear magnetic resonance (NMR) has increasingly been used to study the local structure and dynamics of these complex perovskites.³⁻⁶ NMR spectra of a target nucleus are largely determined by the coupling of its magnetic dipole and electric quadrupole moments with the local magnetic field and electric field gradient, respectively. The interpretation of NMR spectra in complex solid solution perovskites is complicated by the presence of broad spectral features due to disorder. First-principles calculations of electric field gradient⁷ and chemical shielding⁸ tensors can play an important role interpreting NMR spectra in these materials.

Previously we demonstrated a near linear dependence of the chemical shielding tensor $\hat{\sigma}$ on the oxygen nearest neighbor B-O bond distance r_s for the prototypical perovskites BaTiO_3 (BT), SrTiO_3 (ST), PbTiO_3 (PT), and PbZrO_3 (PZ).⁸ The linear dependence was shown to arise from large paramagnetic contributions to σ_x and σ_y principal values (our convention identifies the “ z ” principal axis as that most nearly parallel to the B-O-B bond direction), due to virtual transitions between $\text{O}(2p)$ and unoccupied $\text{B}(nd)$ states. This linear variation is confirmed here for two complex perovskite solid solutions, PZT and PMN.

First-principles chemical shielding calculations have traditionally been done with the embedded cluster approach, using standard quantum chemistry methods⁹⁻¹¹ with gaussian type orbitals (GTO). More recently, the planewave based GIPAW method with PBC has provided an alternative approach. Relatively few calculations for transition metal oxides have been reported using either technique. Here we use complementary calculations with both methods to cross validate convergence with respect to cluster size and termination effects, basis sets, and the accuracy of pseudopotentials (PSPs).

Quantum-chemistry methods can calculate chemical shielding tensors for embedded clusters, using a range of approximations, from Hartree Fock and density functional theory (DFT) with semilocal or hybrid exchange-correlation functionals, to explicitly correlated methods such Moller-Plesset perturbation theory and coupled cluster approaches.¹²⁻¹⁴ The principal difficulties with the embedded cluster approach are controlling size and basis set convergence. Size effects can be monitored by studying increasingly larger clusters. Long-range electrostatic interactions can be handled by embedding the cluster in large arrays of point charges and eliminating depolarizing fields, as described in Ref. 8. Achieving the basis set limit can be problematic in some cases, because atom-centered GTO's do not form a complete orthogonal basis. Nevertheless, basis set convergence is generally well controlled through the use of standardized GTO basis sets.¹⁵ The cluster approach becomes inefficient, however, for complex systems, because separate cluster calculations are usually required for each inequivalent target atom.

GIPAW calculations are naturally adapted to ordered crystalline solids, since size convergence is effectively achieved by using primitive unit cells with well-converged k -point quadrature grids for Brillouin zone integrations. Disordered solids can be treated using supercells. Planewaves form a complete basis, so convergence

to the basis set limit is straightforward. The method applies the projector-augmented-wave (PAW) reconstruction¹⁶ to a conventional PSP calculation to obtain all-electron valence wave functions, which are required for accurate calculations of the chemical shielding. There are two principle issues with the GIPAW method. GIPAW PSPs are more difficult to construct than standard norm-conserving PSPs. To achieve good transferability, they may require multiple partial wave channels and large planewave cutoff energies for some target atoms. The construction of the PAW atomic-like augmentation basis also requires care. To date, GIPAW calculations have been carried out for only a limited number of transition metal oxide systems.^{17,18}

PZT is a homovalent mixture of Ti^{4+} and Zr^{4+} transition metal cations, while PMN is a heterovalent 2:1 mixture of the Nb^{5+} transition metal cation and the Mg^{2+} alkaline earth cation. Both embedded cluster and GIPAW calculations were carried out for PZT, while PMN results were obtained only with the GIPAW method, using PBC. First-principles relaxed structural models were used to simulate PZT and PMN structures.

The remainder of the paper is organized as follows. The theoretical approaches are described in Sec. II. Results and discussion are presented in Secs. III and IV, respectively. We summarize and conclude in Sec. V.

II. THEORETICAL METHODS

The chemical shielding tensor $\hat{\sigma}$ determines the total magnetic field at an atomic nucleus,

$$\mathbf{B} = (1 - \hat{\sigma})\mathbf{B}_{\text{ext}}, \quad (1)$$

where \mathbf{B}_{ext} is the external field. For the systems considered here, $\hat{\sigma}$ is calculated using embedded cluster and GIPAW-PBC methods. The symmetric^{19,20} $\hat{\sigma}$ tensor is determined by its principal axis components, with isotropic and anisotropic parts, conventionally defined as²¹

$$\begin{aligned} \sigma_{\text{iso}} &= \frac{1}{3}(\sigma_x + \sigma_y + \sigma_z) = \frac{1}{3}\text{Tr } \hat{\sigma} \\ \sigma_{\text{ax}} &= \frac{1}{6}(2\sigma_z - \sigma_x - \sigma_y) = \frac{1}{2}(\sigma_z - \sigma_{\text{iso}}) \\ \sigma_{\text{aniso}} &= \frac{1}{2}(\sigma_y - \sigma_x) \end{aligned} \quad (2)$$

As mentioned, our convention for the perovskite structure identifies the “ z ” principal axis as that most nearly parallel to the B-O-B bond direction. NMR measurements of $\hat{\sigma}$ are usually reported with respect to a reference material, where the chemical shift tensor $\hat{\delta}$ is defined as¹³

$$\hat{\delta} = -(\hat{\sigma} - \sigma_{\text{ref}}), \quad (3)$$

with corresponding definitions to those in Eq. 2. The experimental reference for oxygen is liquid H_2O .

The theoretical oxygen reference value $\sigma_{\text{ref}}^{\text{th.}}$ is determined from a linear regression of $\sigma_{\text{iso}}^{\text{expt.}}$ versus $\sigma_{\text{iso}}^{\text{theory}}$.^{18,22}

This yields the relation

$$\delta^{\text{th.}} = -m(\sigma^{\text{th.}} - \sigma_{\text{ref}}^{\text{th.}}). \quad (4)$$

Rather than regarding the slope m as an independent fitting parameter, we set $m = 1$, which leaves $\sigma_{\text{ref}}^{\text{th.}}$ as the only independent parameter. Allowing m to vary yields fits of similar overall quality, but somewhat distorts chemical shift differences between inequivalent oxygen sites within the same material. Constraining $m = 1$ allows better cancellation of errors, due to systematic effects such as the choice of methodological approach or DFT exchange-correlation functional.

A. Embedded cluster calculations

A detailed discussion of this approach is given in Ref. 8. We briefly summarize some of the key features of this method. With central O atoms, embedded clusters consisted of either 21 “quantum” (QM) atoms, $(\text{A}_4\text{B}_2\text{O}_{15})^{14-}$, or 65 QM atoms, $(\text{A}_4\text{B}_{10}\text{O}_{51})^{51-}$. In these clusters, all cation atoms are fully coordinated with QM O atoms. The QM clusters are further surrounded by a large array of point charges, which reproduce the Madelung potential in the QM region.²³ To alleviate artificial polarization of boundary O(2p) states, the nearest-neighbor (nn) and the next-nearest-neighbor cation point charges of boundary O atoms are replaced by “empty” PSPs (ePSPs).^{8,24} Finally, in non-centrosymmetric clusters, depolarizing electric fields are removed by applying an external electric field.⁸

Calculations were performed with the GAUSSIAN computational package,^{9,11} and the chemical shielding tensor was determined using the continuous set of gauge transformations (CSGT) method.^{25,26} Calculations were done using the DFT hybrid B3LYP²⁷, as well as generalized gradient approximations (GGA), using the PW91²⁸ and PBE²⁹ forms. Douglas-Kroll-Hess 2nd order scalar-relativistic calculations were performed on selected systems. Atom-centered GTO basis functions were associated with all the QM atoms. All-electron treatments were used for the O and Ti atoms, while the other QM atoms were represented using scalar-relativistic small core (scalar-RSC) PSPs [also called effective core potentials (ECPs)]. The well-converged GTO basis sets and ECPs used for these calculations are described in Ref. 8 and were taken from the EMSL website.¹⁵

B. GIPAW calculations

Calculations with PBC used the GIPAW functionality of the QuantumESPRESSO (QE) code.³⁰ These calculations are done in two steps. A standard ground state norm-conserving PSP calculation is first performed. This is followed by a linear response calculation in the presence of an external magnetic field. The linear response

TABLE I: Pseudopotential construction parameters, see text for description.

	reference state	r_c (au)	reference energies (Ry)	core correction radius (au)
O	2s²,2p⁶,3d,3s,3p	1.2,1.2,1.5	*,*,0.10,0.10,0.10	0.34
Ti	3s²,3p⁶,3d⁰,4s,4p,4d	0.9,0.9,0.9	*,*,*, -2.73,0.50,0.10	0.53
Pb	6s²,6p⁰,5d¹⁰,7s,7p,6d	2.0,2.4,1.0	*,*,*, -1.00,-0.20,-1.80	0.89
Zr	4s²,4p⁶,4d⁰,5s,5p,5d	1.0,1.2,1.4	*,*,*, -2.45,-2.00,-1.37	0.80
Sr	4s²,4p⁶,4d⁰,5s,5p	1.2,1.3,1.7	*,*, -1.00,-0.72	0.88
Ba	5s²,5p⁶,5d,6s,6p	1.5,1.7,2.0	*,*, -0.95,-0.90,-1.50	1.19
Mg	2s²,2p⁶,3d,3s,3p	0.6,0.6,1.5	*,*,0.3,-1.3,0.1	0.30
Nb	4s²,4p⁶,4d⁰,5s,5p,5d	1.0,1.1,1.3	*,*,*, -3.30,-2.70,-1.27	0.80
K	3s²,3p⁶,3d⁰,4s,4p	1.4,1.5,1.5	*,*,*, -1.50,-0.80	0.50

calculation uses all-electron like valence wave functions, which are represented by planewaves, modified near the nuclei by atomic-like PAW augmentation basis functions. The PAW basis functions are constructed when the PSP is generated, as further discussed below. Calculations reported below used well converged Monkhorst-Pack³¹ Brillouin zone k -point sampling, *e.g.* $6 \times 6 \times 6$ for the prototypical perovskites ST, BT, and PT. Unless otherwise specified, the PBE GGA functional was used in all QE calculations.

All PSPs were constructed using the “ld1” PSP generation code (distributed with QE). All norm-conserving PSPs were scalar-relativistic Troullier-Martins³² type. Table I shows the construction parameters used for all PSPs employed in this paper. The local channel is indicated by boldface type. States that are in italics were generated using a Hamann type³³ reference state. The r_c ’s correspond to the s , p , and d channels respectively. The next column shows the PSP reference energies for the s , p , and d channels. The symbol ‘*’ indicates that the corresponding all-electron eigenvalue was used for this state. It should be noted that these parameters are for the PSP projectors used in the ground state self-consistent total-energy calculations. Parallel to the PSP construction, a second atomic calculation is performed to generate the required GIPAW augmentation basis functions, consisting of all-electron and pseudo partial wave radial functions. The number of GIPAW angular momentum channels was the same as for the PSPs. For all except Pb, O and K, the augmentation basis functions were generated using the corresponding all-electron eigenvalues (*n.b.*, the Ti^{4+} $4d$ state is bound, for example), rather than the values in Table I. For Pb, O and K, the values in Table I were used, except for the Pb $7s$, which used the all-electron eigenvalue. The final column shows the non-linear core-correction radius for each potential. A conservative 350 Ry energy cutoff was used. This could have been reduced by using larger r_c ’s for the metal PSPs. The 350 Ry energy cutoff, while high, was easily tractable for all systems studied in this paper. This cutoff yields chemical shieldings to within about 1 ppm, as indicated by test calculations with other settings.

TABLE II: Comparison of chemical shielding results, using embedded clusters and GIPAW-PBC from QE and Ref. 18. The principle values of the oxygen chemical shielding tensor are presented for the TiO_2 molecule and rutile, cubic ST, cubic BT, and tetragonal PT. All values are from GGA calculations. Embedded cluster results are labeled as C- n , where n is the number of QM atoms in the cluster. The GIPAW-PBC and C-65 calculations were done with relativistic PBE, while the C-21 calculations were done with non-relativistic PW91.

	σ_x	σ_y	σ_z	σ_{iso}
TiO ₂ (molecule)				
Gaussian	-1803	-801	148	-819
GIPAW	-1826	-811	146	-830
TiO ₂ (rutile)				
C-99	-499	-380	-306	-395
GIPAW	-483	-380	-296	-386
SrTiO ₃ (cubic)				
C-21	-353	-353	46	-220
C-65	-403	-403	27	-260
GIPAW	-429	-429	7	-284 / -287 ^a
BaTiO ₃ (cubic)				
C-21	-414	-414	49	-260
C-65	-483	-483	22	-315
GIPAW	-529	-529	-31	-363 / -379 ^b
PbTiO ₃ -axial O (P4mm)				
C-21	-562	-562	123	-334
C-65	-599	-599	67	-377
GIPAW	-630	-630	77	-394
PbTiO ₃ -equatorial O (P4mm)				
C-21	-286	-228	-32	-182
C-65	-365	-277	-35	-226
GIPAW	-398	-284	-23	-235

^aRef. 18 determined σ_{iso} using the experimental structure

^bRef. 18 determined σ_{iso} using the relaxed structure

C. Comparison of methods

Table II shows the comparison between the GIPAW and cluster approach for the TiO_2 molecule, the rutile crystalline solid, as well as some results for prototypical

TABLE III: The derived theoretical oxygen reference value, $\sigma_{\text{ref}}^{\text{th}}$, is used to determine theoretical isotropic chemical shifts from the corresponding calculated isotropic chemical shielding values. Experimental chemical shifts are shown for comparison. The values of $\sigma_{\text{ref}}^{\text{th}}$ are shown in the third row from the bottom of this table. The rms error and maximum deviation of the calculated shifts, compared to experiment, are also shown. Calculated cluster results (21 and 65 QM atoms) with B3LYP and PW91 exchange-correlation are shown together with GIPAW-PBC with PBE exchange-correlation. (PZ experimental chemical shift site assignments were corrected in Ref. 8 and are used here.)

		Expt ^a	Cluster				present ^f	PBC-GIPAW	
			B3LYP		PW91			present	other
			21	65	21	65			
ST (cubic)		467 ± 5	491	477	494	491	491	496	503 ^b
BT (cubic)		546 ± 5	536	537	534	547	570	575	595 ^c
BT (P4mm)									
	O _{ax}	570 ± 5	591		571			579	573 ^d / 611 ^e
	O _{eq}	520 ± 5	515		516			535	563 ^d / 531 ^e
	Δ(O _{ax} – O _{eq})	50	76		56			44	10 / 80
PT (P4mm)									
	O _{ax}	647 ± 2	644	644	608	609	601	606	
	O _{eq}	443 ± 2	449	445	457	455	442	447	
	Δ(O _{ax} – O _{eq})	204	195	199	152	154	159	159	
PZ (Pbam)									
	O1-4g	365 ± 2	357		367			355	
	O1'-4g	351 ± 2	346		356			336	
	O2-8i	356 ± 2	355		364			349	
	O3-4f	329 ± 2	324		336			309	
	O4-4e	408 ± 2	392		399			415	
	Δ(O4 – O1)	43	35		31			60	
	Δ(O4 – O1')	57	47		43			79	
	ΔO4 – O2)	52	38		35			66	
	Δ(O4 – O3)	79	68		63			105	
σ _{ref} ^{th.}		288 ^e	293	238	275	217	207	212	216
RMS error			12	7	16	23	28	20	26
Max Dev ^f			24	10	39	38	46	41	

^aST and BT experimental chemical shift values are from Ref. 6 and the PT and PZ experimental chemical shift values are from Ref. 4.

^bRef. 18 determined σ_{iso} using the experimental structure

^cRef. 18 determined σ_{iso} using the relaxed structure

^dThe ¹⁷O experimental chemical shielding reference is liquid water, $\sigma_{\text{iso}}^{\text{water}} = 287.5$ ppm³⁴

^eMax Dev = max(abs($\delta^{\text{theory}} - \delta^{\text{expt.}}$))

^fUsed $\sigma_{\text{ref}}^{\text{th}}$ determined from linear regression on the same systems as the 65 QM atom cluster-PW91 results (see text).

perovskites. Where available, published GIPAW results from Ref. 18 are also given for comparison.

TiO₂ molecule calculations were for a Ti-O bond length of 1.651 Å and a O-Ti-O angle of 114.2°. With PBC-GIPAW, a 22×24×28 Bohr supercell was used. The Gaussian calculation was for the isolated molecule and used a basis set of cc-pwCVQZ-DK and IGLO-III for Ti and O, respectively. The experimental rutile structure was used for solid TiO₂.³⁵ The PBC-GIPAW calculation used a k -point sampling of 4×4×6. The cluster

method used a O₇₇Ti₂₂ QM cluster with cc-pwCVTZ-DK and 6-311G(2d,p) basis sets for the inner 3 and outer 19 Ti atoms, respectively; IGLO-III and IGLO-II basis sets were used for the inner 15 and outer 52 O atoms, respectively. (Embedding with ePSPs and point charges was done as described above.)

Calculations for the prototypical perovskites in Table II used the experimental structures as described in Ref. 8. PBC-GIPAW used a k -point sampling of 6×6×6. Embedded clusters were constructed as above (Section II A),

and results are given for 21 and 65 QM atom clusters. The 21 QM atom cluster results are from non-relativistic calculations using the PW91 DFT functional. The 65 QM atom clusters are from scalar relativistic PBE calculations. Differences between PW91 and PBE (not shown in the Table) and relativistic effects are small, as expected. Tests on the 65 QM atom ST cluster show that non-relativistic PBE produced $\sigma_{x,y}$ and σ_z values that are $\simeq 6$ and 1.5 ppm more positive, respectively, than PW91. Adding scalar-relativistic effects changed $\sigma_{x,y}$ and σ_z by $\simeq +12$ and $+3$ ppm, respectively, independent of the GGA functional. These effects are negligible for the corresponding chemical shifts, as expected, due to cancellation of errors.

The ST and PT 65 QM atom relativistic PBE $\sigma_{x,y}$ and σ_z are in good agreement with PBC values, differing at most by $\simeq 33$ and 20 ppm respectively. Isotropic values for both systems are within 24 ppm of PBC-GIPAW. A larger discrepancy is seen in BT, where the cluster values are rigidly shifted by about $+50$ ppm. Size effects between the 21 and 65 QM atom results are evident in the table. The 21 QM atom values are more shielded [*i.e.*, more positive (see Eq. (1))] than either the 65 QM atom values or the PBC methods. Rigidly shifting all 21 QM atom brings these into better agreement, indicating good cancellation of errors. This is evident in the chemical shifts shown in Table III in the next section, where 21 and 65 QM atom clusters are seen to give nearly identical chemical shifts.

These results demonstrate that the embedded cluster and PBC-GIPAW approaches produce comparable agreement with measured isotropic chemical shifts, regardless of cluster size and methodology. Differences due to cluster size, DFT functionals, relativistic effects, and PSPs largely cancel in the chemical shifts, *i.e.*, they are absorbed in the constant chemical shielding reference value $\sigma_{\text{ref}}^{\text{th}}$.

III. RESULTS

In this section, we first describe the calculation of the theoretical oxygen chemical shielding reference $\sigma_{\text{ref}}^{\text{th}}$ [Eq. (4)]. As mentioned, this is done using linear regression of the calculated chemical shieldings with the corresponding measured chemical shifts, where available.^{18,22} We next present calculated ^{17}O chemical shifts for two perovskite-based B-site alloys, PZT and PMN, using the derived values of $\sigma_{\text{ref}}^{\text{th}}$.

A. Determination of the theoretical ^{17}O chemical shielding reference

A linear regression was separately evaluated for the PBC and embedded cluster calculations.^{18,22} Additionally for the clusters, separate regressions were performed for different cluster sizes and DFT functionals. Table III

shows derived $\sigma_{\text{ref}}^{\text{th}}$ values for each case, along with the rms error and maximum deviation in the isotropic chemical shifts. The table compares the resulting calculated isotropic chemical shifts to the measured values. As in Ref. 8, experimental structures were used for all systems except PZ. For PZ, experimental lattice parameters from neutron scattering measurements were used together with internal coordinates determined from first-principles calculations.³⁶

Calculated cluster results (21 and 65 QM atoms) with B3LYP and PW91 exchange-correlation are shown together with GIPAW-PBC with PBE exchange-correlation. The last column shows other GIPAW results, where available. For the 65 QM clusters, $\sigma_{\text{ref}}^{\text{th}}$ is derived from a more limited set of calculations, as shown in the Table. For comparison, the effect of this to be only a few ppm. B3LYP results are seen to give slightly better agreement with experiment. Using the same exchange-correlation treatment, both the 21 and 65 atom QM clusters are seen to give nearly identical chemical shifts. The values of $\sigma_{\text{ref}}^{\text{th}}$ in Table III are used below to determine the theoretical chemical shifts for PZT and PMN in Tables IV and V. Given the small difference between the PW91 and PBE GGA functionals and cancellation effects in chemical shifts, both PW91 and PBE are labeled as GGA in all further results below.

B. Results for $\text{Pb}(\text{Zr}_{1-x}\text{Ti}_x)\text{O}_3$ (PZT) and $\text{Pb}(\text{Mg}_{1/3}\text{Nb}_{2/3})\text{O}_3$ (PMN)

PZT is a homovalent mixture of Ti^{4+} and Zr^{4+} transition metal cations, while $\text{Pb}(\text{Mg}_{1/3}\text{Nb}_{2/3})\text{O}_3$ (PMN) is a heterovalent 2:1 mixture of the Nb^{5+} transition metal cation and the Mg^{2+} alkaline earth cation. Both embedded cluster and GIPAW calculations were carried out for PZT, while PMN results were obtained only with the GIPAW method, using PBC.

Disordered PZT 50/50 was modeled using first-principles relaxed structures⁷ with different imposed B-site ordering and symmetry: i) [001] ordering parallel to the ferroelectric polarization, with tetragonal P4mm symmetry ($a \times a \times 2c$; $c/a = 1.045$); ii) [001] ordering perpendicular to the [100] ferroelectric polarization, with orthorhombic P2mm symmetry ($a' \times a \times 2a$; $a'/a = 1.04$); iii) [111] ordering (rocksalt B sublattice) parallel to the ferroelectric polarization, with R3m symmetry. Theoretical PZT isotropic, axial, and anisotropic chemical shifts are summarized in Table IV. [As mentioned, the axial and anisotropic components in Eq. (2) were calculated using the convention that the “ z ” principal axis is that most nearly parallel to the B-O-B bond direction of the target O atom.] For comparison, results for ST, BT, PT and PZ are reproduced from Table III. For each inequivalent target O atom in the above structural models, the corresponding 21 QM atom embedded cluster was used to calculate the chemical shielding tensor with both B3LYP and GGA

TABLE IV: Calculated oxygen isotropic, axial and anisotropic components (ppm) of the chemical shift tensor for three PZT 50/50 structural models from Ref. 7. The notation B--O--B indicates O atoms with two equidistant nn B atoms, and B-O--B indicates an O atom with one short and one long nn B bond. For cluster-GGA results, numbers in parenthesis show the difference with GIPAW. For cluster-B3LYP results, numbers in square brackets show the difference with cluster-GGA values. For cases where $\delta_{\text{aniso}} = 0$ by symmetry, this is indicated by a dash.

	δ_{iso}			δ_{ax}			δ_{aniso}		
	Cluster B3LYP	GGA	GIPAW GGA	Cluster B3LYP	GGA	GIPAW GGA	Cluster B3LYP	GGA	GIPAW GGA
ST (cubic)	491 [-3]	494 (-2)	496	-144 [-11]	-133 (12)	-145	—	—	—
BT (cubic)	536 [2]	534 (-41)	575	-170 [-16]	-154 (12)	-166	—	—	—
BT (P4mm)									
Oax (Ti-O--Ti)	591 [20]	571 (-8)	579	-207 [-24]	-183 (3)	-186	—	—	—
Oeq (Ti--O--Ti)	515 [-1]	516 (-19)	535	-155 [-14]	-140 (7)	-147	-24 [2]	-26 (15)	-41
PT (P4mm)									
Oax (Ti-O--Ti)	644 [35]	608 (2)	606	-257 [-29]	-228 (8)	-236	—	—	—
Oeq (Ti--O--Ti)	449 [-8]	457 (10)	447	-85 [-10]	-75 (31)	-106	-22 [7]	-29 (28)	-57
PZ(Pbam)									
O1-4g (Z--O--Z)	357 [-10]	367 (12)	355	-75 [-5]	-70 (20)	-90	-33 [1]	-34 (12)	-46
O1'-4g (Z--O--Z)	346 [-10]	356 (20)	336	-65 [-4]	-61 (21)	-81	-14 [2]	-16 (11)	-27
O2-8i (Z-O--Z)	355 [-9]	364 (16)	349	-81 [-4]	-77 (14)	-91	-4 [1]	-5 (2)	-7
O3-4f (Z--O--Z)	324 [-11]	336 (26)	309	-47 [-4]	-43 (9)	-52	-15 [-1]	-14 (3)	-17
O4-4e (Z--O--Z)	392 [-6]	399 (-16)	415	-137 [-7]	-130 (36)	-166	-14 [1]	-15 (11)	-26
PZT (P4mm)									
O1(Zr--O--Zr)	352 [-9]	361 (33)	328	-72 [-6]	-66 (20)	-85	-16 [-4]	-12 (-4)	-8
O2(Zr-O--Ti)	398 [7]	391 ^a (-19)	410	-126 [-8]	-118 (17)	-135	—	—	—
O3(Ti--O--Ti)	418 [-18]	436 (9)	427	-76 [-11]	-65 (21)	-86	-59 [4]	-63 (38)	-101
O4 (Ti-O--Zr)	679 [40]	639 (13)	626	-266 [-34]	-232 (14)	-246	—	—	—
PZT (P2mm)									
O1(Zr--O--Zr)	358 [-9]	367 (19)	348	-80 [-6]	-74 (22)	-96	-36 [2]	-38 (20)	-59
O2(Zr-O--Zr)	401 [-4]	405 (-1)	407	-124 [-6]	-118 (18)	-137	-34 [2]	-36 (9)	-44
O3(Ti--O--Ti)	408 [-11]	419 (24)	395	-65 [-8]	-57 (17)	-74	-6 [5]	-1 (26)	-27
O4(Ti-O--Ti)	668 [39]	629 (12)	617	-264 [-32]	-232 (6)	-238	-49 [3]	-46 (8)	-54
O5(Ti-O--Zr)	400 [-6]	406 (21)	385	-81 [-9]	-72 (20)	-92	-29 [-3]	-32 (22)	-55
PZT (R3m)									
O1(Zr-O--Ti)	394 [-7]	401 (0)	401	-90 [-6]	-84 (23)	-107	-3 [1]	-2 (1)	-3
O2(Ti-O--Zr)	466 [-1]	467 (11)	456	-127 [-13]	-114 (21)	-135	-2 [1]	-1 (-1)	-1

^aThis cluster-GGA calculation used a smaller Pb cc-pVDZ basis, rather than cc-pVTZ, due to convergence difficulty with the larger basis.

exchange-correlation. Results from PBC-GIPAW with GGA exchange-correlation are also shown. Chemical shifts were determined using the corresponding values of $\sigma_{\text{ref}}^{\text{th}}$ in Table III. The GGA 21 QM atom embedded cluster and PBC-GIPAW RMS errors differ by 4 ppm. As seen in Tables III, the 21 QM atom embedded cluster

chemical shifts are also in excellent agreement with those from the larger 65 QM atom cluster.

PMN PBC-GIPAW calculations were based on a low symmetry ($3 \times 2 \times 2$) 60-atom perovskite supercell structure with relaxed internal coordinates,³⁷ with B-site cations arranged according to the random-site model.³⁸

X-ray patterns of well-annealed PMN samples indicate a homogeneous average structure, which exhibits rocksalt-like 1:1 B-site ordering, which is well described by the random-site model. Locally, the random-site model corresponds to B-site [111] planes, alternating between pure Nb and mixed Nb/Mg layers. Thus there are twice as many Nb-O-Mg as Nb-O-Nb O-sites in the 60-atom supercell, since the Mg atoms all reside in the mixed [111] planes. Similarly, there are no Mg-O-Mg O-sites. Unlike earlier models, the random-site model satisfies charge neutrality locally. The previously accepted space-charge model was based on the apparent inability to fully anneal samples.³⁸ The 60-atom perovskite supercell structure,³⁷ used in the present calculations, is consistent with the random-site model. Grinberg *et al.*³⁷ found good agreement between this relaxed 60-atom supercell structure and pair distribution functions (PDFs) obtained by neutron scattering experiments.³⁹ This indicates that this structural model reasonably represents the local structure in PMN. Calculations for PMN were done only with PBC-GIPAW, and the results are shown in Table V.

IV. DISCUSSION

As previously noted in Ref. 8, there is a large anisotropy between the $\sigma_{x,y}$ and σ_z principal values in Table II. The $\sigma_{x,y}$ principal values are large and negative (deshielded), while σ_z values tend to be considerably smaller and positive (shielded). (As mentioned, the “ z ” principal axis is identified as that most closely aligned with the B-O-B bond direction of the target O atom.) The present calculations show that this anisotropy is also found in PZT and PMN and is reflected in the large δ_{ax} values (Eq. 2) in Tables IV and V.

As shown in Ref. 8 for prototypical perovskites, the large δ_{ax} values are due to paramagnetic contributions to $\sigma_{x,y}$ from virtual transitions between O(2p) and unoccupied B(nd) states. The p-d hybridization contributes predominantly to $\sigma_{x,y}$, due to O atoms having only two nearest neighbors in perovskites, with linearly arranged B-O-B structural units. As the B-O-B bond distances vary, large variations in the chemical shielding can occur, resulting in a strong dependence on r_s . We find a similar dependence for the PZT and PMN alloy systems.

A. PZT

Figure 1 plots PZT isotropic and axial chemical shifts as a function of r_s , the shortest B-O bond length of the targeted O atom. The B3LYP 21 QM atom cluster results from Table IV are plotted. For comparison, results for ST, BT, PT, and PZ and from experiment are also shown.⁸ The dashed straight lines are the linear fits to the calculated results for these prototypical perovskites, taken from Ref. 8. A plot of PBC-GIPAW results from Table IV (not shown) is very similar, which

is consistent with the generally good agreement of the chemical shift results in the Table between the two calculational approaches. A nearly linear dependence on r_s (with slope ~ 850 ppm/Å) is seen in both δ_{iso} and δ_{ax} , across all the systems studied. The axial shift is plotted as $2\delta_{ax} = \delta_z - \delta_{iso}$ (Eq. 2) to emphasize that the linear dependence is largely due to $\delta_{x,y}$, while δ_z has a much weaker dependence on r_s , as previously noted for the prototypical perovskites.⁸ As seen in the figure, the calculated PZT 50/50 results follow the same trends as in Ref. 8.

$\text{Pb}(\text{Zr}_{1-x}\text{Ti}_x)\text{O}_3$ NMR ^{17}O magic angle spinning (MAS) central peak spectra were presented by Baldwin *et al.*⁴ for a range of concentrations x . Tabulated chemical shifts were given only for the endpoint PT and PZ compounds (reproduced here in Table III), whose spectra consist of well-defined narrow peaks. MAS removes broadening due to chemical shift anisotropy in powder samples, but only partly averages second-order quadrupolar broadening. The narrow peaks in the endpoint PT and PZ compounds indicate that electric field gradients (EFGs) at the ^{17}O nuclei are small.⁴ This is consistent with first-principles calculations of O EFGs.^{7,36} Indeed, the ^{17}O peak positions are within a few ppm of the experimental isotropic chemical shifts.⁴ There are two inequivalent O atoms in PT, two “equatorial” O_{eq} (which has two equidistant nn Ti atom) and one “axial” O_{ax} atom (which has one short and one long Ti-O bond). A narrow peak at 443 ppm has twice the (integrated) relative intensity of the peak at 647 ppm, and these were assigned to the O_{eq} and O_{ax} atoms, respectively. These are in good agreement with the calculated results in Table III. The B3LYP calculation accurately reproduces this splitting, while GGA underestimates it by $\simeq 45$ ppm. In PZ, there are five inequivalent O sites, which corresponds to five MAS peaks, centered near 350 ppm, within $\pm \sim 40$ ppm. Measured and calculated values in Table III are in good agreement.

At intermediate Ti and Zr concentrations, the spectra in Fig. 3 of Ref. 4 show that only a few of the narrow endpoint peaks persist. As Zr is added to PT, the narrow 647 ppm PT peak decreases quickly in intensity. It can no longer be observed in the $x = 0.55$ sample. A broad feature, between about 350 and 450 ppm is fully developed near $x \simeq 0.50$, with narrower embedded features at $\simeq 370$ and 430 ppm. This broad feature distribution of inequivalent O-sites in the disordered PZT solid solution samples. The 430 ppm feature, which is close to the PT O_{eq} 447 ppm peak, is observed to persist down to 25% Ti concentration. Baldwin *et al.*⁴ assign the 430 ppm feature to a site similar to that of the PT O_{eq} atom, *i.e.* a locally Ti- O_{eq} -Ti (undimerized) chain-like configuration. They further suggest that this peak could indicate Ti clustering on a spatial scale of at least two unit cells in PZT.

Our results suggest an alternative explanation for the persistence of the observed 430 ppm feature. Our calcu-

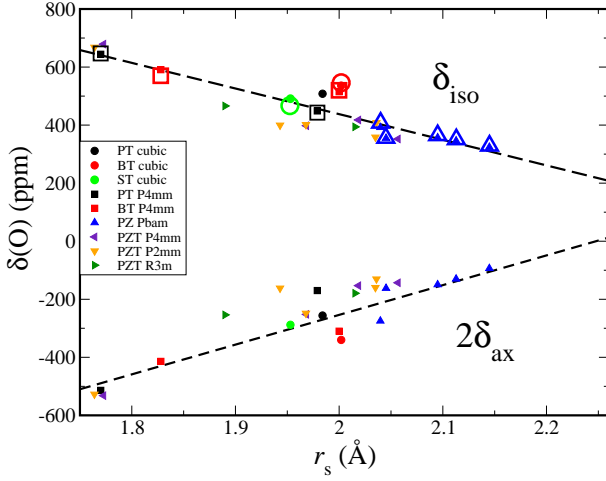


FIG. 1: (Color online) Calculated PZT oxygen isotropic δ_{iso} and axial $2\delta_{\text{ax}}$ chemical shifts (B3LYP 21 QM atom cluster values from Tables IV), plotted as a function of r_s , the shortest B-O bond length of the targeted O atom. For comparison, calculated results for ST, BT, PT, and PZ and from experiment (hollow symbols) are also shown.⁸ The dashed straight lines are linear fits to calculated values for ST, BT, PT, and PZ from Ref. 8.

lations show similar chemical shifts for a range of B-O-B' environments, with r_s ranging between $\sim 2.0 - 2.1$ Å in all the PZT 50/50 structural models, as seen in Table IV and Fig. 1. Thus Ti clustering need not be invoked to explain the persistence of the 430 ppm feature in the measured spectra.

The apparent disappearance, at intermediate concentrations, of the 647 ppm peak does, however, indicate a reduced occurrence of a PT-like O_{ax} site with a short 1.77 Å Ti-O bond. We find such a site only in the relaxed P4mm and P2mm PZT 50/50 simulations. The P4mm and P2mm models have [100] type B-site ordering. The absence of the 647 ppm peak in the measurements indicates that local occurrences of [100] type B-site ordering are rare. Instead, the lack of the 647 ppm peak in our R3m PZT 50/50 simulations suggests that local rocksalt-like B-site ordering is more prevalent in disordered PZT. This conclusion is also supported by the R3m structural model having the lowest total energy of all the structural models by ~ 23 mRy.⁷ Moreover, the calculated Ti EFG's for 50/50 R3m were significantly smaller and in better agreement with measured values, than the other B-site orderings.⁷

Baldwin *et al.*⁴ also remark a narrow 287 ppm peak that appears in their $x = 0.48$ sample. This peak is broader in $x = 0.55$ and $x = 0.25$ samples and is absent in PZ. These authors note that $x = 0.48$ is the composition corresponding to the morphotropic phase boundary (MPB) and conjecture that the 287 ppm peak evidences a new oxygen environment in a distinct crystalline monoclinic phase, which has been suggested to bridge the MPB.⁴ They suggest that the new environment at

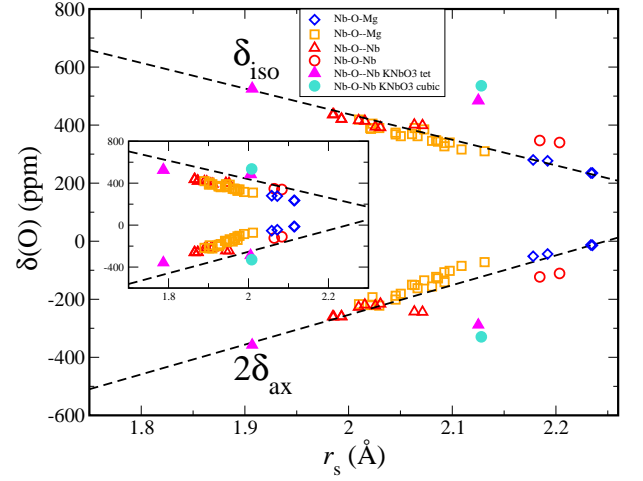


FIG. 2: (Color online) GIPAW calculated PMN oxygen isotropic δ_{iso} and axial $2\delta_{\text{ax}}$ chemical shifts, plotted as a function of r_s . The PMN chemical shifts are from Table V, and the symbols indicate the B-O-B' configuration, using the convention in that table. For comparison, results for cubic and tetragonal KNbO_3 are also shown. The dashed lines are the same as that in Fig. 1. As plotted, the r_s values have been increased by 0.12 Å (see text). The unshifted values are shown in the inset.

$x = 0.48$ is a Ti-O-Zr site, which becomes ordered in the crystallographic sense as the long-range order of the monoclinic phase is established. As indicated by Fig. 1, isotropic chemical shifts near 287 ppm are associated with large $r_s \simeq 2.15$ Å. As most Zr-O bond lengths are larger than those of Ti-O in the PZ and PZT 50/50 structural models, the 287 ppm feature could also be attributed to Zr-O-Zr sites with bond lengths distributed near $\simeq 2.15$ Å.

B. PMN

PMN, by contrast with PZT, is a heterovalent 2:1 mixture of the Nb^{5+} transition metal cation and the Mg^{2+} alkaline earth cation. Figure 2 plots $\text{Pb}(\text{Mg}_{1/3}\text{Nb}_{2/3})\text{O}_3$ (PMN) isotropic and axial chemical shifts (GIPAW results from Table V) as a function of r_s , the shortest B-O bond length of the targeted O atom. As plotted, the PMN r_s values, have been increased by 0.12 Å for both δ_{iso} and δ_{ax} , as further discussed below. The unshifted values are plotted in the inset. The dashed lines are the same as that in Fig. 1. With the 0.12 Å rigid shift for all O-sites, the PMN chemical shifts are seen to follow the same linear trend as in the homovalent B-site systems in Fig. 1. For Nb-O-Mg coordinated O-atoms, r_s is taken as the Nb-O bond length, since the hybridization mechanism does not apply to Mg, which has no low-lying unoccupied d-states. (As mentioned, the linear dependence is due to paramagnetic contributions to δ_{xy} from virtual transitions between O(2p) and unoccupied B(nd)

states.) We are not aware of published NMR ^{17}O spectra for PMN.

Although the linear dependence of δ_{iso} and δ_{ax} in Fig. 2 have the same slope as the homovalent B-site systems, a $0.12 \text{ \AA } r_s$ offset is needed for the PMN values to fall on the same line. As mentioned, the linear dependence reflects variations in the magnitude of the paramagnetic O(2p)-Nb(4d) hybridization contributions to the $\delta_{x,y}$ principal values. This indicates that the effective r_s is controlled by the spatial extent of the paramagnetic screening currents. The Nb^{5+} cation could be expected to modify the spatial extent of these currents, compared to the B^{4+} cations in the homovalent systems, due to the larger electrostatic attraction of the Nb^{5+} cation. The 0.12 \AA offset in PMN renormalizes, in effect, the strength of the O(2p)-Nb(4d) hybridization. This observation would appear to indicate that for these systems the r_s -dependence of $\delta_{x,y}$ is given by $\delta_{x,y} = m(r_s - r_0)$, where the slope m is nearly the same for all transition-metal coordinated O atoms in perovskites, while the intercept r_0 depends on other factors, such as the ionic charge of the nearest neighbor cation. To further examine this, we performed GIPAW calculations for cubic and tetragonal KNbO_3 ,⁴⁰ which are also plotted in Fig. 2. While the tetragonal axial O values (short Nb-O r_s) are consistent with the linear trend, the KNbO_3 tetragonal equatorial and cubic O results (two equidistant Nb-O bonds) show significant deviations. [Similar deviations occur in Fig. 1 for the tetragonal equatorial and cubic O BT results. We note that both K and Ba have larger crystalline ionic Shannon⁴¹ radii, 1.78 and 1.75 \AA , respectively, than Sr or Pb, 1.58 and 1.63 \AA , respectively.] Smaller deviations are also seen in the two largest r_s values for the PMN oxygen atoms with two nearly equidistant Nb atoms, but for somewhat larger values of r_s than in KNbO_3 . In the case of heterovalent B-site perovskites, the covalency of A-site atoms could also be important, as indicated by the smaller deviations, for long r_s , in PMN compared to KNbO_3 . These observations warrant further investigation to clarify these issues.

PMN is an end-point of the solid-solution series $(x)\text{PbTiO}_3 - (1-x)\text{Pb}(\text{Mg}_{1/3}\text{Nb}_{2/3})\text{O}_3$ (PMN-PT). In the 60-atom PMN structural model, there are no Nb-O bonds as small as the short Ti-O_{ax} bond $\simeq 1.7 \text{ \AA}$ in PT, which is associated with its high degree of tetragonality ($c/a = 1.065$). This short bond corresponds to the large $\delta_{\text{iso}} \simeq 640 \text{ ppm}$, which is also seen in the P4mm and P2mm PZT structural models, both of which also show a high degree of tetragonality. The tetragonality of PMN-PT decreases as the Ti concentration is reduced from PT-rich compositions, and the average symmetry switches from tetragonal to rhombohedral at the mor-

photropic phase boundary (MPB) $x \simeq 0.35$. The largest piezoelectric response is typically achieved at concentrations near the MPB.⁴² Polarization rotation has been proposed as the origin of the large piezoelectric response at the MPB, via intermediate monoclinic phases,^{43–45} where the tetragonality increases as the polarization rotates from [111] to [100] (pseudocubic) directions, with applied electric field along a pseudocubic axis. Increased tetragonality, compared to PT, has been seen in some other perovskite based solid solutions, such as some Bi based materials.^{46,47} The present calculations indicate that ^{17}O NMR chemical shift measurements could be a useful probe in this regard, as increased tetragonality is accompanied by shortened transition-metal/oxygen bonds.

V. SUMMARY

First-principles oxygen NMR chemical shift tensors were calculated for PZT and PMN, which are representative, respectively, of homovalent and heterovalent perovskite-structure B-site alloys. Quantum chemistry methods for embedded clusters and the GIPAW method for periodic boundary conditions were used. Results from both methods are in good agreement for PZT and prototypical perovskites. PMN results were obtained using only GIPAW. Both isotropic and axial chemical shift components were found to vary approximately linearly as a function of the nearest-distance transition-metal/oxygen bond length, r_s . Using these results, we argue against Ti clustering in PZT, as conjectured from recent ^{17}O NMR measurements. Our findings indicate that ^{17}O NMR measurements, coupled with first-principles calculations, can be an important probe of local structure in complex perovskite solid solutions.

VI. ACKNOWLEDGMENTS

This research was supported by Office of Naval Research grants N00014-08-1-1235 and N00014-09-1-0300. DLP acknowledges partial support from a Virginia Space Grant Consortium Graduate Research Fellowship. Support for computations was provided in part by National Science Foundation TeraGrid resources at the National Center for Supercomputing Applications (NCSA) under grant number TG-DMR100024. Additional computational resources were provided by the Center for Piezoelectric by Design. We acknowledge useful discussions with Gina Hoatson and Robert L. Vold.

¹ M. Dawber, K. Rabe, and J. Scott *Rev. Mod. Phys.*, vol. 77, no. 4, p. 1083, 2005.

² J. Scott *Science*, vol. 315, p. 954, 2007.

³ D. H. Zhou, G. L. Hoatson, R. L. Vold, and F. Fayon *Phys.*

- Rev. B*, vol. 69, p. 134104, 2004.
- ⁴ A. Baldwin, P. A. Thomas, and R. Dupree *J. Phys.: Condens. Matter*, vol. 17, p. 7159, 2005.
 - ⁵ M. Vijayakumar, G. L. Hoatson, and R. L. Vold *Phys. Rev. B*, vol. 75, p. 104104, 2007.
 - ⁶ R. Blinc, V. V. Laguta, B. Zalar, M. Itoh, and H. Krakauer *J. Phys.: Condens. Matter*, vol. 20, p. 085204, 2008.
 - ⁷ D. Mao, E. J. Walter, H. Krakauer, and Z. Wu *Phys. Rev. B*, vol. 76, p. 014105, 2007.
 - ⁸ D. L. Pechkis, E. J. Walter, and H. Krakauer *J. Chem. Phys.*, vol. 131, no. 18, p. 184511, 2009.
 - ⁹ M. J. Frisch, G. W. Trucks, H. B. Schlegel, and *et al.*, "Gaussian 98, Revision A.11.4." Gaussian, Inc., Pittsburgh PA, 2002.
 - ¹⁰ M. J. Frisch, G. W. Trucks, H. B. Schlegel, and *et al.*, "Gaussian 03, Revision C.02." Gaussian, Inc., Wallingford, CT, 2004.
 - ¹¹ M. J. Frisch, G. W. Trucks, H. B. Schlegel, and *et al.*, "Gaussian 09, Revision A.02.," Gaussian, Wallingford CT, 2009.
 - ¹² T. Helgaker, M. Jaszunski, and K. Ruud *Chem. Rev.*, vol. 99, no. 1, p. 293, 1999.
 - ¹³ M. Kaupp, M. Bühl, and V. Malkin, *Calculation of NMR and EPR Parameters: Theory and Applications*. Wiley-VCH, Weinheim, 2004.
 - ¹⁴ J. Vaara *Phys. Chem. Chem. Phys.*, vol. 9, p. 5399, 2007.
 - ¹⁵ K. L. Schuchardt, B. T. Didier, T. Elsethagen, L. Sun, V. Gurumoorthi, J. Chase, J. Li, and T. L. Windus, "Basis set exchange: A community database for computational sciences," *J. Chem. Inf. Model.*, vol. 47, no. 3, pp. 1045–1052, 2007.
 - ¹⁶ C. G. V. de Walle and P. E. Blöchl *Phys. Rev. B*, vol. 47, p. 4244, 1993.
 - ¹⁷ L. Truffandier, M. Paris, and F. Boucher *Phys. Rev. B*, vol. 76, p. 035102, 2007.
 - ¹⁸ D. S. Middlemiss, F. Blanc, C. J. Pickard, and C. P. Grey *J. Magn. Reson.*, vol. 204, p. 1, 2010.
 - ¹⁹ R. F. Schneider *J. Chem. Phys.*, vol. 48, p. 4905, 1968.
 - ²⁰ F. Anet and D. J. O'Leary *Concepts in Magn. Reson.*, vol. 3, p. 193, 1991.
 - ²¹ J. F. Baugher, P. C. Taylor, T. Oja, and P. J. Bray *J. Chem. Phys.*, vol. 50, p. 4914, 1969.
 - ²² T. Charpentier, S. Ispas, M. Profeta, F. Mauri, and C. J. Pickard *J. Phys. Chem. B*, vol. 108, p. 4147, 2004.
 - ²³ M. K. Klintenberg, S. E. Derenzo, and M. J. Weber *Comput. Phys. Commun.*, vol. 131, p. 120, 2000.
 - ²⁴ N. W. Winter, R. M. Pitzer, and D. K. Temple *J. Chem. Phys.*, vol. 86, p. 3549, 1987.
 - ²⁵ T. A. Keith and R. F. W. Bader *Chem. Phys. Lett.*, vol. 210, p. 223, 1993.
 - ²⁶ J. R. Cheeseman, G. W. Trucks, T. A. Keith, and M. J. Frisch *J. Chem. Phys.*, vol. 104, p. 5497, 1996.
 - ²⁷ A. D. Becke *J. Chem. Phys.*, vol. 98, p. 5648, 1993.
 - ²⁸ K. Burke, J. P. Perdew, and Y. Wang, *Electronic Density Functional Theory: Recent Progress and New Directions*. Plenum, 1998.
 - ²⁹ J. P. Perdew, K. Burke, , and M. Ernzerhof *Phys. Rev. Lett.*, vol. 77, p. 3865, 1996.
 - ³⁰ P. Giannozzi, S. Baroni, N. Bonini, M. Calandra, R. Car, C. Cavazzoni, D. Ceresoli, G. L. Chiarotti, M. Cococcioni, I. Dabo, A. Dal Corso, S. de Gironcoli, S. Fabris, G. Fratesi, R. Gebauer, U. Gerstmann, C. Gougousis, A. Kokalj, M. Lazzeri, L. Martin-Samos, N. Marzari, F. Mauri, R. Mazzarello, S. Paolini, A. Pasquarello, L. Paulatto, C. Sbraccia, S. Scandolo, G. Sclauszero, A. P. Seitsonen, A. Smogunov, P. Umari, and R. M. Wentzcovitch *J. Phys.: Condens. Matter*, vol. 21, p. 395502, 2009.
 - ³¹ H. J. Monkhorst and J. D. Pack *Phys. Rev. B*, vol. 13, p. 5188, 1976.
 - ³² N. Troullier and J. L. Martins *Phys. Rev. B*, vol. 43, p. 1993, 1991.
 - ³³ D. R. Hamann *Phys. Rev. B*, vol. 40, p. 2980, 1989.
 - ³⁴ R. E. Wasylishen and D. Bryce *J. Chem. Phys.*, vol. 117, p. 10061, 2002.
 - ³⁵ S. C. Abrahams and J. L. Bernstein *J. Chem. Phys.*, vol. 55, p. 3206, 1971.
 - ³⁶ M. D. Johannes and D. J. Singh *Phys. Rev. B*, vol. 71, p. 212101, 2005.
 - ³⁷ I. Grinberg and A. M. Rappe *Phys. Rev. B*, vol. 70, p. 220101, 2004.
 - ³⁸ P. K. Davies and M. A. Akbas *J. Phys. Chem. Solids*, vol. 61, p. 159, 2000.
 - ³⁹ T. Egami, W. Dmowski, M. Akbas, and P. K. Davies, "Local structure and polarization in Pb containing ferroelectric oxides," vol. 436, p. 1, AIP, 1998.
 - ⁴⁰ C.-Z. Wang, R. Yu, and H. Krakauer *Phys. Rev. B*, vol. 54, p. 11161, 1996.
 - ⁴¹ R. D. Shannon, "Revised effective ionic radii and systematic studies of interatomic distances in halides and chalcogenides," *Acta Crystallographica Section A*, vol. 32, pp. 751–767, Sep 1976.
 - ⁴² S.-E. Park and T. R. Shrout *J. Appl. Phys.*, vol. 82, p. 1804, 1997.
 - ⁴³ B. Noheda and D. E. Cox *Phase Transitions*, vol. 79, p. 5, 2006. (See references within).
 - ⁴⁴ H. Fu and R. Cohen *Nature*, vol. 403, p. 281, 2000.
 - ⁴⁵ Z. Wu and H. Krakauer *Phys. Rev. B*, vol. 68, p. 014112, Jul 2003.
 - ⁴⁶ M. R. Suchomel and P. K. Davies *Appl. Phys. Lett.*, vol. 86, p. 262905, 2005.
 - ⁴⁷ D. M. Stein, M. R. Suchomel, and P. K. Davies *Appl. Phys. Lett.*, vol. 89, p. 132907, 2006.

TABLE V: GIPAW calculated oxygen isotropic, axial and anisotropic components (ppm) of the chemical shift tensor for PMN. A 60-atom supercell with relaxed internal coordinates was used.³⁷ The B-O--B' bond notation is the same as in Table IV; bond lengths are categorized as equidistant if they differ by less than 0.05 Å.

	Nb-O Å	B'-O Å	δ_{iso}	δ_{ax}	δ_{aniso}
<hr/>					
Nb-O-Mg					
	2.11	2.09	235	-6	-5
	2.11	2.09	235	-7	-2
	2.06	2.08	280	-26	-47
	2.07	2.09	277	-22	-43
<hr/>					
Nb-O--Mg					
	1.89	2.06	419	-109	-27
	1.90	2.07	405	-97	-11
	1.90	2.09	390	-110	-25
	1.90	2.11	387	-110	-31
	1.91	2.11	390	-111	-83
	1.93	2.08	362	-91	-7
	1.93	2.09	368	-94	-10
	1.93	2.10	374	-100	-83
	1.94	2.13	369	-75	-36
	1.94	2.18	390	-75	-17
	1.95	2.11	362	-81	-11
	1.95	2.18	385	-67	-18
	1.96	2.05	346	-78	-29
	1.96	2.12	348	-61	-44
	1.97	2.05	338	-71	-36
	1.97	2.10	343	-64	-11
	1.97	2.13	327	-53	-13
	1.98	2.06	340	-51	-47
	1.99	2.13	316	-43	-7
	2.01	2.06	310	-36	-39
<hr/>					
Nb-O--Nb					
	1.86	2.23	436	-130	-21
	1.87	2.14	421	-130	-3
	1.87	2.14	421	-129	-8
	1.87	2.23	437	-130	-18
	1.89	2.20	416	-114	-27
	1.90	2.20	414	-110	-24
	1.91	2.11	394	-111	-23
	1.91	2.11	392	-108	-18
	1.94	2.03	401	-122	-8
	1.95	2.01	399	-122	-11
<hr/>					
Nb-O-Nb					
	2.06	2.09	347	-62	-9
	2.08	2.08	340	-56	-11
<hr/>					